

A Theoretical Study on Surfactant Adsorption Kinetics: Effect of Bubble Shape on Dynamic Surface Tension

Ming-Wei Yang,[†] Hsien-Hung Wei,[‡] and Shi-Yow Lin^{*,†}

Department of Chemical Engineering, National Taiwan University of Science and Technology, 43 Keelung Road, Sec. 4, Taipei, 106 Taiwan, and Department of Chemical Engineering, National Cheng Kung University, No. 1 University Road, Tainan, 701 Taiwan

Received July 3, 2007. In Final Form: September 19, 2007

A planar or spherical fluid–liquid interface was commonly assumed on studying the surfactant adsorption kinetics for a pendant bubble in surfactant solutions. However, the shape of a pendant bubble deviates from a sphere unless the bubble's capillary constant is close to zero. Up to date, the literature has no report about the shape effect on the relaxation of surface tension due to the shape difference between a pendant bubble and a sphere. The dynamic surface tension (DST), based on the actual shape of a pendant bubble with a needle, of the diffusion-controlled process is simulated using a time-dependent finite element method in this work. The shape effect and the existence of a needle on DST are investigated. This numerical simulation resolves also the time-dependent bulk surfactant concentration. The depth of solution needed to satisfy the classical Ward–Tordai infinite-solution assumption was also studied. For a diffusion-controlled adsorption process, bubble shape and needle size are two major factors affecting the DST. The existence of a needle accelerates the bulk diffusion for a small bubble; however, the shape of a large pendant bubble decelerates the bulk diffusion. An example using this method on the DST data of C₁₂E₄ is illustrated at the end of this work.

1. Introduction

Dynamic surface tension (DST) at the liquid–fluid interface is important to many applications, such as foams, coatings, and bioprocessings.^{1–5} For a surfactant solution with a concentration below the critical micelle concentration (cmc), the DST of a freshly created surface is governed by the diffusion step from the bulk phase to the sublayer and the adsorption step from the sublayer to the fluid surface. With the local equilibrium assumption, the diffusion-controlled mechanism has been applied to many surfactants.

DST reflects the interfacial transport phenomena of a surfactant solution. For a diffusion-controlled process, the classical Ward–Tordai equation first accounts for the bulk molecular diffusion onto a planar surface. Numerical solutions are generally needed, since most of the adsorption isotherms are nonlinear, especially on interpreting DST data that is extracted from a nonplanar interface.

A common approach to this calculation is applying the trapezoidal rule approximation to the Ward–Tordai equation.^{6,7} The planar diffusion-controlled process can also be solved by the finite difference or the finite element method.^{8,9} Another way for solving this problem is the regular perturbation method.¹⁰ Analytical solutions from the perturbation method are useful in

the initial adsorption stage, and they have been compared to the numerical solutions. Many surfaces of interest or those that have been utilized are, however, not planar.

Droplets and bubbles were frequently encountered in industrial problems as well as in scientific measurements of interfacial tension. In such cases, a spherical interface usually results in a better approximation than a planar one.¹¹ Asymptotic analytical solutions have been also developed in various spherical drop systems with a finite solution depth.¹² The actual geometry of the pendant drop also plays an important role in the dynamic surface tension phenomenon. Yang and Gu¹³ had simulated the surfactant mass transport for the case of a pendant drop in air and studied the shape effect of the liquid drop.

The kinetic barrier may play an important role on DST relaxation like bulk diffusion does on surfactant adsorption processes. Some analytical expressions have been derived for the process of mixed kinetic–diffusive control.^{14–17}

The pendant bubble tensiometer has emerged as a very accurate and useful tool for measuring the surface tension of a fluid–liquid interface.^{6,18–20} Diffusion from the bulk solution to the bubble surface is commonly approximated as the diffusion to a spherical surface.^{6,21}

For a spherical bubble inside a surfactant solution, surfactant molecules diffuse radially toward the bubble surface. Compared

* To whom correspondence should be addressed. Telephone: +886-2-2737-6648. Fax: +886-2-2737-6644. E-mail: sylin@mail.ntust.edu.tw.

[†] National Taiwan University of Science and Technology.

[‡] National Cheng Kung University.

(1) Miller, R.; Fainerman, V. B.; Wüstneck, R.; Krägel, J.; Trukhin, D. V. *Colloids Surf., A* **1998**, *131*, 225.

(2) Beverung, C. J.; Radke, C. J.; Blanch, H. W. *Biophys. Chem.* **1999**, *81*, 59.

(3) Baugot, F.; Langevin, D.; Lenormand, R. *J. Colloid Interface Sci.* **2001**, *239*, 501.

(4) Miller, R.; Fainerman, V. B.; Makievski, A. V.; Krägel, J.; Grigoriev, D. O.; Kazakov, V. N.; Sinyachenko, O. V. *Adv. Colloid Interface Sci.* **2000**, *86*, 39.

(5) Lu, J. J.; Yu, L. M. Y.; Cheung, W. W. Y.; Policova, Z.; Li, D.; Hair, M. L.; Neumann, A. W. *Colloids Surf., B* **2003**, *29*, 119.

(6) Lin, S. Y.; McKeigue, K.; Maldarelli, C. *AIChE J.* **1990**, *36*, 1785.

(7) Miller, R.; Kretzschmar, G. *Colloid Polym. Sci.* **1980**, *258*, 85.

(8) Miller, R. *Colloid Polym. Sci.* **1981**, *259*, 375.

(9) Liao, Y. C.; Franses, E. I.; Basaran, A. J. *Colloid Interface Sci.* **2003**, *258*, 310.

(10) McCoy, B. J. *Colloid Polym. Sci.* **1983**, *261*, 535.

(11) Mysels, K. J. *J. Phys. Chem.* **1982**, *86*, 4648.

(12) Filippov, L. K.; Filippova, N. L. *J. Colloid Interface Sci.* **1997**, *187*, 352.

(13) Yang, C.; Gu, Y. *Langmuir* **2004**, *20*, 2503.

(14) Danvo, K. D.; Valkovska, D. S.; Kralchevsky, P. A. *J. Colloid Interface Sci.* **2002**, *251*, 18.

(15) Borwankar, R. P.; Wasan, D. T. *Chem. Eng. Sci.* **1983**, *38*, 1637.

(16) Liggerieri, L.; Ravera, F.; Ferrari, M.; Passerone, A.; Miller, R. *J. Colloid Interface Sci.* **1997**, *186*, 46.

(17) Eastoe, J.; Dalton, J. S. *Adv. Colloid Interface Sci.* **2000**, *85*, 103.

(18) Lin, S. Y.; Tsay, R. Y.; Lin, L. W.; Chen, S. I. *Langmuir* **1996**, *12*, 6530.

(19) Lin, S. Y.; Lu, T. L.; Hwang, W. B. *Langmuir* **1995**, *11*, 555.

(20) Hsu, C. T.; Chang, C. H.; Lin, S. Y. *Langmuir* **2000**, *16*, 1211.

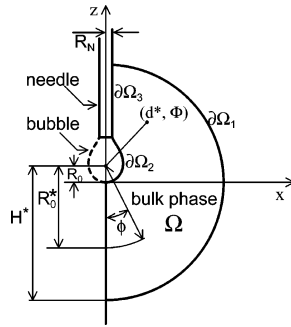


Figure 1. Coordinate system of a pendant bubble in surfactant solution: Ω = bulk domain in which the time-dependent mass transport of surfactant is considered; $\partial\Omega_1$ = an imaginary spherical boundary surface; $\partial\Omega_2$ = the imaginary sublayer right next to the pendant surface; and $\partial\Omega_3$ = solution boundary adjacent to the needle.

with a planar surface, the curvature of the bubble surface speeds up the diffusive flux. The rate of mass transport therefore accelerates due to the surface curvature.²² It may fail to describe the DST of a spherical bubble if one neglects the geometric effect of a bubble and assumes a planar surface. Ignoring the surface curvature could cause a significant error in evaluating the bulk diffusivity of surfactant molecules.²³

Assuming a spherical interface does give a much better prediction on the DST for a pendant bubble than a planar one. Two questions come to mind. Can a spherical interface predict the same DST as that for a real bubble surface? What is the difference in the relaxation of DST and bulk concentration for a spherical interface and for an exact bubble surface?

Of course, the deviation between the spherical and bubble surfaces depends upon the capillary constant (B) and bubble volume (V). The DST for surfactants diffusing onto a pendant bubble surface may depart clearly from that for a spherical one, especially for a large pendant bubble that has a large absolute capillary number.

The existence of a needle may cause another significant error on simulating the DST data. Pendant bubbles are used to being generated, and therefore hanged, on the tip of a straight (or U type) cylindrical needle. The bulk diffusive flux at the region near the needle may have a significant contribution to the adjacent bubble surface. A larger flux therefore results at the region close to the three-phase contact circle. It is important to include the needle effect on fitting the DST data to describe more precisely the actual experimental environment.

In this work, a theoretical simulation based on an actual pendant bubble, hanging on the tip of a needle, is performed for calculating the diffusion-controlled DST due to the mass transport of a surfactant onto a freshly created surface. A time-dependent finite element method is applied to simulate the bulk diffusion and the kinetic adsorption/desorption processes numerically. With the aim of the present modeling, surfactant adsorption onto pendant bubbles can be analyzed more precisely. This numerical simulation resolves further the time-dependent surfactant concentration in the bulk phase and the depth of solution needed to satisfy the Ward–Tordai infinite-solution assumption.

(21) Stebe, K.; Lin, S. Y. Dynamic surface tension and surfactant mass transfer kinetics: measurement techniques and analysis. In *Handbook of surfaces and interfaces of materials: Surface and interface analysis and properties*; Nalwa, H. S., Ed.; Academic Press: San Diego, CA, 2001; Vol. 2, Chapter 2.

(22) Ferri, J. K.; Lin, S. Y.; Stebe, K. J. *J. Colloid Interface Sci.* **2001**, *241*, 154.

(23) Hsu, C. T.; Chang, C. H.; Lin, S. Y. *Langmuir* **1997**, *13*, 6204.

2. Time-Dependent Mass Transport

The x - z planar projection of the pendant bubble model is plotted in Figure 1. In this study, it is considered a three-dimensional diffusion and a surfactant adsorption onto an actual pendant bubble surface from a static bulk phase (denoted by Ω). The bulk phase contains an initially uniform distribution of surfactant, and a pendant bubble is suddenly created on the tip of a needle at $t = 0$. The pendant bubble deforms slightly while the surfactant molecules diffuse and adsorb onto the surface. The flow in the bubble adjacent to the bulk phase may be induced by the shape deformation. For a surfactant solution with a concentration below the cmc, an incompressible bulk phase and a constant diffusivity can be assumed. The general equation of convective diffusion for the surfactant exchange in bulk fluid can be expressed as follows:

$$\frac{\partial C}{\partial t} + \mathbf{u} \cdot \nabla C = D \nabla^2 C \quad \text{in } \Omega \quad (1)$$

where t is the time, C is the bulk concentration, D is the diffusivity, and \mathbf{u} is the velocity in bulk phase. The convective diffusion equation can be reduced to a dimensionless form by introducing a characteristic length L and a characteristic flow velocity u_0 . Here, L represents the length along which the major change in concentration takes place and u_0 represents the velocity of the bulk fluid. Equation 1 can be written as follows:

$$\frac{\partial C^*}{\partial t^*} + Pe(\mathbf{u}^* \cdot \nabla C^*) = \nabla^2 C^* \quad \text{in } \Omega \quad (2)$$

where $C^* = C/C_0$, $t^* = Dt/L^2$, and $u^* = u/u_0$. In terms of Cartesian coordinates, the dimensionless coordinates can be expressed as $x^* = x/L$, $y^* = y/L$, and $z^* = z/L$. The dimensionless ratio $Pe = u_0 L/D$ is known as the Peclet number. The relationship between the convective and the diffusive transfer of surfactants is, therefore, described by Peclet number.

In a common pendant bubble experiment, the bubble is hanged on the tip of a needle in static bulk fluid. The air is enclosed in the bubble, and the bubble keeps a nearly constant volume during the measurement. Therefore, the bulk velocity just comes from the bubble deformation. The deformation-induced flow in bulk fluid is rather slow. In general, a small Peclet number will be found in a common pendant bubble experiment. Therefore, the convective term in eq 2 can be neglected.²⁴ In this case, the concentration distribution in the bulk phase is caused primarily by molecular diffusion; at sufficiently low Pe , mass transfer by convection is negligible.

This work tries to study the roles of the bubble shape and needle on the DST. The effect of bubble shape change on DST during the measurements is not significant and is neglected here. More discussion on this issue is detailed later in the Discussion section.

For a stationary and well-deformed pendant bubble, the convective diffusion can be simplified as follows:

$$\frac{\partial C}{\partial t} = D \nabla^2 C \quad \text{in } \Omega \quad (3)$$

The boundary and initial conditions are

$$C = C_0 \quad \text{on } \partial\Omega_1; t \geq 0 \quad (4a)$$

(24) In a common DST experiment, Ca and Re are $O(10^{-9})$ and $O(10^{-4})$ from an order analysis, respectively. The effects of fluid motions are rather small, and the bubble can be assumed to be hydrostatic. Further discussion is detailed in a manuscript accepted by *Colloids Surf., A* (ms. ref. no.: COLSUA-14994).

$$\frac{d\Gamma}{dt} = \mathbf{n} \cdot D\nabla C \quad \text{on } \partial\Omega_2; t \geq 0 \quad (4b)$$

$$C = C_0 \quad \text{in } \Omega; t = 0 \quad (4c)$$

$$\Gamma = 0; C = 0 \quad \text{on } \partial\Omega_2; t = 0 \quad (4d)$$

$$C = C_0 \quad \text{on } \partial\Omega_3; t = 0 \quad (4e)$$

$$\mathbf{n} \cdot D\nabla C = 0 \quad \text{on } \partial\Omega_3; t \geq 0 \quad (4f)$$

An imaginary spherical boundary, $\partial\Omega_1$, far away from the bubble surface is assumed to remain at a constant concentration C_0 during the whole adsorption process (eq 4a). The position of the boundary $\partial\Omega_1$ is set far away from the bubble surface $\partial\Omega_2$.

Boundary condition 4b describes the rate of change of the surface concentration Γ , being related to the bulk concentration gradient ∇C on the imaginary sublayer $\partial\Omega_2$. Note that $\partial\Omega_2$ can be viewed as the surface of the pendant bubble and ∇C changes with time. Therefore, the rate of the change of surface concentration varies with time also during the whole process. The outward normal of the pendant bubble surface is denoted by \mathbf{n} in eq 4b. The dependence between Γ and C on the imaginary sublayer $\partial\Omega_2$ is unique and is described by the adsorption isotherm when the process is of diffusion control.

In this work, the contribution from bulk flow and surface diffusion was neglected and only the bulk diffusion was considered in the mass transport process.²⁵ The inhomogeneity of the surface concentration was neglected, since the experimental bubble profiles in this study can always be fitted perfectly by the Young–Laplace equation.²⁶ Note that the deviations of the best-fitting, for the fit between the experimental bubble and theoretical bubble from the Young–Laplace equation, of a bubble in pure water and in surfactant solution are nearly identical in this work.

At the beginning of the process, the bulk phase contains a uniform concentration distribution (eq 4c) except the imaginary sublayer $\partial\Omega_2$ has a zero concentration. For a clean surface adsorption process, the bubble is suddenly created, and the bubble surface is fresh and clean with zero surface concentration. Therefore, a zero sublayer concentration at $t = 0$ on $\partial\Omega_2$ (eq 4d) is assumed to satisfy the adsorption isotherm.

The solution adjacent to the needle wall is represented by boundary $\partial\Omega_3$. It is assumed that the needle is in contact with the surfactant solution for a long time before a bubble is generated. Therefore, the concentration on boundary $\partial\Omega_3$ equals to the initial bulk concentration C_0 at $t = 0$ (eq 4e). No surfactant molecules cross through the needle (eq 4f) during the whole process.

Boundaries $\partial\Omega_1$, $\partial\Omega_2$, and $\partial\Omega_3$ enclose the region for the computational bulk fluid phase. The area enclosed by $\partial\Omega_1$, $\partial\Omega_2$, and $\partial\Omega_3$ shown in Figure 1 revolves about the z -axis to generate a 3-D computational geometric model of a pendant bubble for the finite element method. On the theoretical simulation, it is considered only 30°, as shown in Figure 2, about the z -axis in this enclosed region to have a better convergence. More discussion on the accuracy is given later on this simplification.

3. The Finite Element Method

The solution of PDEs on complicated geometries can rarely be expressed in terms of elementary functions. The finite element

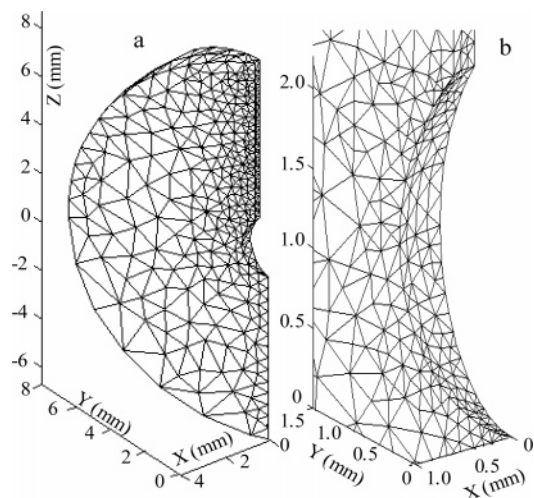


Figure 2. Illustration of mesh: (a) mesh with 1793 elements for demonstration and (b) parts of the mesh near the bubble surface with a total of 5264 mesh elements in the whole computational domain.

method (FEM), the so-called discretization of the original problem, approximates the PDE problem with a finite number of unknown parameters. This method involves introducing finite elements or shape functions that describe the possible forms of the approximate solution for the original PDE problem. The complicated geometry is partitioned into small units of a simple shape via the mesh of the finite element method. The 3-D FEM is usually utilized to treat complicated geometry or to obtain more accurate results without any simplification.^{27,28}

In this work, the FEM for pendant bubbles considers a general 3-D system. In the spatial discretization of the computational domain, tetrahedron mesh elements are constructed. The faces, edges, and corners are called mesh faces, mesh edges, and mesh vertices, respectively. The boundaries in the domain are partitioned into triangular boundary elements (mesh faces).

A Galerkin finite element method^{27,28} with quadratic basis functions for discretization is used to expand the PDE for each mesh element on Ω at any time. The concentration profile is expanded in terms of a series of quadratic basis functions ϕ_i :

$$C(x, y, z, t) = \sum_i c_i(t) \phi_i(x, y, z) \quad (5)$$

where c_i is the undetermined coefficient. The Galerkin weighted residuals of eq 3 can be constructed with quadratic basis functions ϕ_i and integrated over the computational domain.

$$\iiint_{\Omega} \phi_i \left[\frac{\partial}{\partial x} \left(D \frac{\partial C}{\partial x} \right) + \frac{\partial}{\partial y} \left(D \frac{\partial C}{\partial y} \right) + \frac{\partial}{\partial z} \left(D \frac{\partial C}{\partial z} \right) - \frac{\partial C}{\partial t} \right] dV = 0 \quad (6)$$

Each of the first three terms in the brackets in eq 6 can be integrated by parts using the Green–Gauss theorem. Thus, eq 6 can be written as follows:

(25) Ca/E has a value of $O(10^{-7})$ from an order analysis. Surface concentration and surface tension are therefore uniform. Further discussion is detailed in a manuscript accepted by *Colloids Surf., A* (ms. ref. no.: COLSUA-14994).

(26) Miller, R.; Joos, P.; Fainerman, V. B. *Adv. Colloid Interface Sci.* **1994**, *49*, 249.

(27) Rao, S. S. *The Finite Element Method in Engineering*, 2nd ed; Pergamon Press: New York, 1986.

(28) Reddy, J. N. *An Introduction to The Finite Element Method*, 2nd ed.; McGraw-Hill: New York, 1993.

$$-\int_{\Omega} \int \int D \left[\frac{\partial \phi_i}{\partial x} \frac{\partial C}{\partial x} + \frac{\partial \phi_i}{\partial y} \frac{\partial C}{\partial y} + \frac{\partial \phi_i}{\partial z} \frac{\partial C}{\partial z} \right] dV + \int_{\partial \Omega} \int D \phi_i \left[\frac{\partial C}{\partial x} n_x + \frac{\partial C}{\partial y} n_y + \frac{\partial C}{\partial z} n_z \right] dA - \int_{\Omega} \int \int \phi_i \left(\frac{\partial C}{\partial t} \right) dV = 0 \quad (7)$$

By applying eq 5 and the boundary conditions (eq 4a and b), eq 7 can be expressed in matrix form as

$$[K]c + [K^{(1)}]c' = [P] \quad (8)$$

where

$$K_{ij} = \int_{\Omega} \int \int D \left[\frac{\partial \phi_i}{\partial x} \frac{\partial \phi_j}{\partial x} + \frac{\partial \phi_i}{\partial y} \frac{\partial \phi_j}{\partial y} + \frac{\partial \phi_i}{\partial z} \frac{\partial \phi_j}{\partial z} \right] dV \quad (9)$$

$$K_{ij}^{(1)} = \int_{\Omega} \int \int \phi_i \phi_j dV \quad (10)$$

$$P_{ij} = \int_{\partial \Omega_2} \int \left(\frac{d\Gamma}{dt} \right) \phi_i dA \quad (11)$$

Equation 8 represents the element equation of a mesh element. The assembly of these equations on the whole domain leads to the following ordinary differential equation (ODE):

$$[K]c + [K^{(1)}]c' = P \quad (12)$$

The assembled ODEs of eq 12 can be solved with the initial conditions (eq 4c and d) and boundary condition (eq 4a).

The set of governing equations, eqs 3 and 4, are solved numerically by the Galerkin finite element method with the Lagrange–quadratic basis functions for discretization. An iterative method, GMRES,²⁹ is then used to solve the integration system. The convergence criterion is based on the residual. To get a more accurate surface concentration, one has to work carefully on the mesh size for the region near the bubble surface. More discussions on the accuracy and mesh size are given later.

4. Adsorption Equations and Dynamic Surface Tension

To complete the solution for the surface concentration, the adsorption kinetics has to be specified. The Langmuir isotherm was used in this work to describe the surfactant adsorption onto the bubble surface. At equilibrium, the rate of change of surface concentration vanishes and the adsorption isotherm is given by

$$\frac{\Gamma}{\Gamma_{\infty}} = x = \frac{C}{C + a} \quad (13)$$

where Γ_{∞} and a are the two parameters of the Langmuir adsorption isotherm which represent the maximum surface concentration and surfactant activity, respectively.

For a diffusion-controlled process, the kinetic adsorption process is much faster than the bulk diffusion one. Thus, the bulk concentration in the sublayer and the surface concentration at the bubble surface keep at equilibrium at any time. When the surfactant solution is considered to be an ideal one, the Gibbs adsorption equation and the equilibrium isotherm allow for the calculation of the surface tension in terms of

$$\gamma - \gamma_0 = \Gamma_{\infty} RT \ln(1 - x) \quad (14)$$

where γ_0 is the clean surface tension.

It is considered only the diffusion-controlled surfactant mass transport in this work. Therefore, the concentration profile in the bulk phase can be obtained from eq 12 by FEM. Note that the subsurface concentration depends upon the position of the bubble (i.e., function of turning angle ϕ , as shown in Figure 1). The surface concentration Γ is then calculated from eq 13, the adsorption isotherm, since the process is of diffusion control. Γ is therefore a function of position also; that is, depends upon ϕ . The surface tension is then found out by eq 14 from the average surface concentration for the whole bubble surface. The variation of surface concentration on the bubble profile is assumed to be negligible in this work. The subsurface concentration at different positions is assigned to be an average concentration calculated from eq 13 with the average surface concentration. This average subsurface concentration is then used on the next iteration.

5. Pendant Bubble Profile

Theoretical shapes of pendant bubbles are derived according to the Young–Laplace equation, which relates the surface tension, the radii of curvature, and the pressure difference across the curved fluid interface:^{30,31}

$$\gamma[1/R_1 + 1/R_2] = \Delta P \quad (15)$$

where γ is the surface tension, R_1 and R_2 are the two principal radii of curvature of the bubble surface, and ΔP is the pressure difference across the interface. Equation 15 can be recast as a set of three first-order differential equations for the spatial positions x and z and turning angle ϕ of the interface as a function of the arc length s , and then integrated with boundary conditions $x(0) = z(0) = \phi(0) = 0$.

The first-order differential equations can be changed into the following forms by applying the dimensionless variables $x^* = x/R_0$, $z^* = z/R_0$, and $s^* = s/R_0$.

$$d\phi/ds^* = 2 + Bz^* - \sin \phi/x^* \quad (16a)$$

$$dx^*/ds^* = \cos \phi \quad (16b)$$

$$dz^*/ds^* = \sin \phi \quad (16c)$$

where B is the capillary constant ($=\Delta\rho g R_0^2/\gamma$), $\Delta\rho$ is the density difference between the fluid phases, g is the gravitational acceleration, and R_0 is the radius of curvature at the apex. The equations are subject to the boundary conditions $x^*(0) = z^*(0) = \phi(0) = 0$. Equation 16 was integrated by using the variable order Adams–Bashforth–Moulton PECE solver in MATLAB initialized with an approximate solution:

$$x^* = s^* \quad (17a)$$

$$z^* = 2[1 - J_0((-B)^{1/2}x^*)]/(-B) \quad (17b)$$

$$\phi = 2[J_1((-B)^{1/2}x^*)]/(-B)^{1/2} \quad (17c)$$

Equation 17 is valid near the apex where $\phi \ll 1$.³² Here, $J_n(x^*)$ is the Bessel function of the first kind.

(30) Lin, S. Y.; Chang, H. C.; Lin, L. W.; Huang, P. Y. *Rev. Sci. Instrum.* **1996**, *67*, 2852.

(31) Rotenberg, Y.; Boruvka, L.; Neumann, A. W. *J. Colloid Interface Sci.* **1983**, *93*, 169.

(32) Huh, C.; Reed, R. L. *J. Colloid Interface Sci.* **1983**, *91*, 472.

(29) Saad, Y.; Schultz, M. H. *SIAM J. Sci. Stat. Comput.* **1986**, *7*, 856.

Table 1. Representative Simulation Parameters^a

no.	C_0/a	x_c	γ_e (mN m ⁻¹)	$-B$	R_0 (mm)	H^* (mm)	h_p (mm)	h_{sp} (mm)	h_{p-b} (mm)	A (mm ²)	V (mm ³)	V_s (mm ³)
1	0.5	0.33	64.9	0.10	0.81	8.0	11.6	2.0	1.9	7.7	2.4	2874
2	0.5	0.33	64.9	0.20	1.15	10.0	11.6	2.5	2.3	18.4	7.9	5805
3	0.5	0.33	64.9	0.29	1.39	11.3	11.6	2.7	2.6	31.5	16.6	8473
4	2.5	0.71	50.3	0.10	0.72	5.4	5.0	1.3	1.2	5.8	1.6	972
5	2.5	0.71	50.3	0.20	1.01	6.7	5.0	1.5	1.3	11.8	5.3	1922
6	2.5	0.71	50.3	0.30	1.24	7.6	5.0	1.7	1.6	25.0	11.9	2885
7	10	0.91	30.5	0.10	0.56	3.0	1.6	0.63	0.58	2.8	0.6	185
8	10	0.91	30.5	0.20	0.79	3.7	1.6	0.72	0.66	8.0	2.4	371
9	10	0.91	30.5	0.33	1.01	4.3	1.6	0.80	0.71	16.8	6.7	607

^a Parameters used: $\Gamma_\infty = 7 \times 10^{-10}$ mol/cm², $a = 4 \times 10^{-10}$ mol/cm³, $D = 5 \times 10^{-6}$ cm²/s, and R_n (outer radius of the needle) = 0.535 mm. A = bubble surface area, V = bubble volume, V_s = solution volume, and H^* is calculated from V_s in which there is 30 times the surfactant of $\Delta\Gamma_e$.

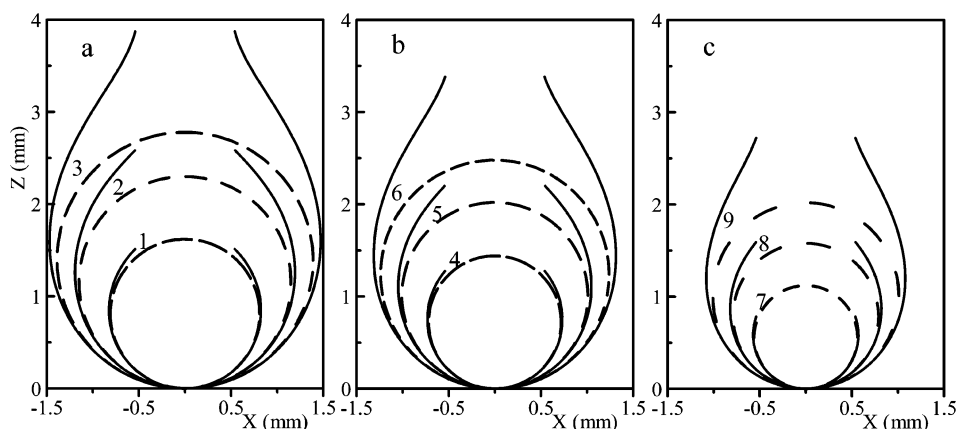


Figure 3. Comparison between the pendant–bubble profiles with R_0 (solid curves) on the tip of the needle and the spherical bubble with $R_i = R_0$ (dashed curves). The numbers 1–9 indicate cases 1–9 in Table 1. C_0/a = (a) 0.5, (b) 2.5, and (c) 10.

6. Simulation Framework

Pendant Bubble. Table 1 illustrates the representative simulation parameters of the pendant bubble system used in this study. The concentrations chosen in the study intend to cover the actual working range applied in the dynamic experiments of surfactant adsorption. To evaluate the effects of bulk concentration on the adsorption kinetics, dimensionless concentrations (C_0/a) of 0.5, 2.5, and 10 are studied. Note that a is the surfactant activity (eq 13).

The deformation of bubbles also depends upon the drop volume and capillary constant. Pendant bubbles with three different capillary constants, $-B = 0.1, 0.2,$ and ~ 0.3 , and three different R_0 (radius of curvature at apex) are studied to evaluate the effect of bubble shape on the dynamic surface tension. The bubble profiles studied in this work are shown in Figure 3.

The equilibrium surface tension at different bulk concentrations can be calculated from eqs 13 and 14. In this study, the needle is fixed (assuming $R_n = 0.535$ mm = half of the o.d. of a needle of gauge no. 19), and the R_0 of the pendant bubble can be obtained from the given B and equilibrium γ . As mentioned above, the profiles of pendant bubbles depend only on B and R_0 . With known values of B , R_0 , and R_n , the boundary $\partial\Omega_2$ of the computational domain Ω can be generated by the numerical procedure detailed in above section. The surface areas and volumes of the generated pendant bubbles are listed in Table 1.

To construct the computational domain Ω for FEM, an imaginary boundary $\partial\Omega_1$ is essential. In this study, the imaginary boundary $\partial\Omega_1$ was chosen based on a mass balance of surfactant to simulate the infinite boundary condition, which is used in the classical spherical case.^{6,21} The Ω is designed to contain surfactant around 25–30 times the absorbed surfactant at bubble surfaces

when the system has reached the equilibrium state. Under this condition, the acceleration of the rate of mass transport due to the assumption of fixed bulk concentration on $\partial\Omega_1$ will not affect the DST profiles. If Ω contains surfactant less than 10 times the absorbed surfactant, the effect on DST due to the assumption of fixed concentration on $\partial\Omega_1$ may be significant. A normal distance for Ω containing 30 times the absorbed surfactant on $\partial\Omega_2$ is defined as H^* . In other words, H^* (listed in Table 1) is a normal distance between $\partial\Omega_1$ and the bubble surface $\partial\Omega_2$ in the apex direction.

Spherical Bubble. To examine the spherical mass transport model and to investigate the effect of the needle on DST, two simulations on a spherical surface were performed. The first one considers a perfect spherical air–water interface, in which the spherical interface is completely enclosed by surfactant solution without a needle attached to it. The second one considers a bubble of spherical shape attached to the tip of a syringe needle with radius $R_n = 0.535$ mm.

Mass transport in the solution bulk phase was commonly simplified to diffusion onto a sphere.⁶ An implicit equation for the evolution of surface concentration to a spherical bubble of radius b is⁶

$$\Gamma(t) = \frac{D}{b} [C_0 t - \int_0^t C_s(\tau) d\tau] + 2\sqrt{\frac{D}{\pi}} [C_0 \sqrt{t} - \int_0^{\sqrt{t}} C_s(t - \tau) d\sqrt{\tau}] \quad (18)$$

The last two items in the above equation are the same as the Ward–Tordai planar expression. The equation becomes the Ward–Tordai planar expression when b (bubble radius) is infinity.

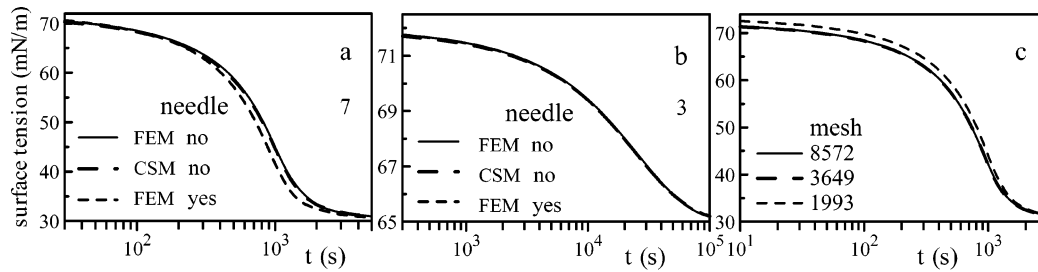


Figure 4. (a and b) DST profiles from (i) the CSM (dashed curves) and (ii) the FEM predictions for spherical bubbles without (solid curves) and with (dotted curves) the needle for case 7 (a) and case 3 (b). (c) DST profiles of a pendant bubble using FEM with 8572 (solid curve), 3649 (dashed curve), and 1993 (dotted curve) mesh elements for case 7 in Table 1.

Adsorption Depth. For a planar fluid–liquid interface, an adsorption depth is commonly defined based on the mass balance: $VC_0 = Ah_pC_0 = A\Gamma_e$. A bulk solution within one adsorption depth contains the same amount of surfactant as that which adsorbs at the fluid–liquid interface, when the system reaches equilibrium.³³ Therefore, $h_p = \Gamma_e/C_0$ for a planar surface.

For a spherical bubble, the adsorption depth can be defined in a similar way in the radial direction. Consider the same mass balance of surfactant for a spherical surface: $(4\pi/3)(R^{*3} - R_i^3)C_0 = 4\pi R_i^2\Gamma_e$. R_i is the radius of the spherical bubble, and R^* defines a bulk domain, containing the same amount of surfactant as that which adsorbs at the spherical interface. Therefore, the adsorption depth in the radial direction for a spherical bubble is defined as: $h_{sp} = R^* - R_i$.

For a pendant bubble, the adsorption depth in the radial direction can be expressed as $h_{pb} = R_0^* - R_0$. R_0 is the radius of curvature at the apex of a pendant bubble, and R_0^* is evaluated from a similar mass balance of surfactant: $(V/R_0^3)(R_0^{*3} - R_0^3)C_0 = A\Gamma_e$, where A and V are the surface area and the volume of pendant bubble. In other words, R_0^* is the equivalent radius of curvature in the apex direction for a pendant bubble (see Figure 1). These three different adsorption depths are listed in Table 1 for the cases shown in Figure 3.

7. Simulation Results

FEM Validation. The spherical FEM implementing the above algorithms has been conducted for the cases shown in Figure 3. Dynamic surface tension profiles from the FEM and the classical spherical model (CSM, eq 18) are demonstrated in Figure 4a and b for comparison. The DST profiles for the FEM without a needle (solid curves) and those for the CSM (dashed curves) are nearly identical. The implemented geometrical model, mesh element, time-stepping algorithm, and discretization method of the FEM are therefore verified.

Figure 4c shows DST profiles of a pendant bubble using the FEM with different mesh numbers. The DST with 1993 mesh elements shows a slower relaxation (higher tension) than those with 3649 or 8572 elements. However, the cases for 3649 and 8572 elements resulted in nearly exact same DST profiles. Note that the mesh size decreases with increasing mesh number, and a lower mass flux results when the mesh size is too large. To have an accurate DST profile, over 8600 mesh elements are utilized in all the simulations in this work.

Needle Effect. In the pendant bubble method, bubbles are commonly generated at the tip of a syringe needle for DST measurements. The existence of a needle may affect the surfactant mass transport due to the significant volume of the needle. Two representative DST profiles for spherical bubbles with or without a needle are shown in Figure 4a and b. Note that the spherical

bubble of case 7 is small compared with that of case 3 (as shown in Figure 3), but the needle diameter is the same for both cases. The data in Figure 4a show that the DST for run 7 with a needle (dotted curve) relaxes faster clearly than that without a needle (dashed curve). For a bigger bubble (case 3), the existence of a needle does not result a faster relaxation of DST (Figure 4b). The data in Figure 4 (a and b) imply that the existence of a needle may accelerate the rate of mass transport when the size of the needle is comparable to the size of bubble. This is because the tip of the needle covers parts of the surface of the spherical bubble. The surfactant within the solution in the neighborhood of the needle cannot diffuse across the needle. Therefore, surfactants in this region diffuse and adsorb directly onto the bubble surface adjacent to the needle tip.

In other words, when R_n (radius of the needle) is close to R_i (radius of the spherical bubble; $R_i = R_b$ for the CSM), this acceleration becomes significant, and the DST shows a faster relaxation. If R_i is much larger than R_n , the deviation is nearly negligible. Therefore, a larger bubble and/or a smaller needle are recommended on measuring the DST when one applies a pendant bubble technique. One can then use the CSM to simulate the measured DST profiles on studying the adsorption kinetics when the spherical bubble is large enough.

Pendant Bubble. The FEM simulations on DST for pendant bubbles and spherical bubbles with a needle are shown in Figure 5. The bubble profiles are shown in Figure 3, and solution properties are listed in Table 1. Data in Figure 5a and d show that the DSTs of pendant bubbles (solid curves) are very close to the DSTs of spherical bubbles with a needle (dashed curves) when the absolute capillary constant is small (i.e., when a pendant bubble is close to parts of a sphere). Figure 5a and d shows cases 1 and 7 in Table 1, where $-B = 0.1$.

When $-B$ becomes large, that is, the pendant bubble deviates significantly from a spherical shape, the DST relaxation profiles of pendant bubbles are slightly higher than those of spherical bubbles with a needle. Figure 5 (b, c, and f) shows cases 2, 3 and 9 in Table 1, where $-B = 0.2$ and ~ 0.3 . The DST of a pendant bubble (solid curve) with a larger $-B$ departs more significantly from that of a spherical bubble (dashed curve).

Figure 5d shows again that the needle effect on DST, that is, the difference between the pendant bubble (solid curve, with needle, p-b) and classical spherical model (CSM, dotted curve, without needle), is significant for a small pendant bubble. DST from the CSM shows a slower relaxation for a small bubble (with a smaller $-B$). Recall that the DST profiles from a pendant bubble and from a spherical bubble with a needle are very close to each other when the bubble is small. The faster surface tension relaxation for a small pendant bubble (or a spherical bubble with

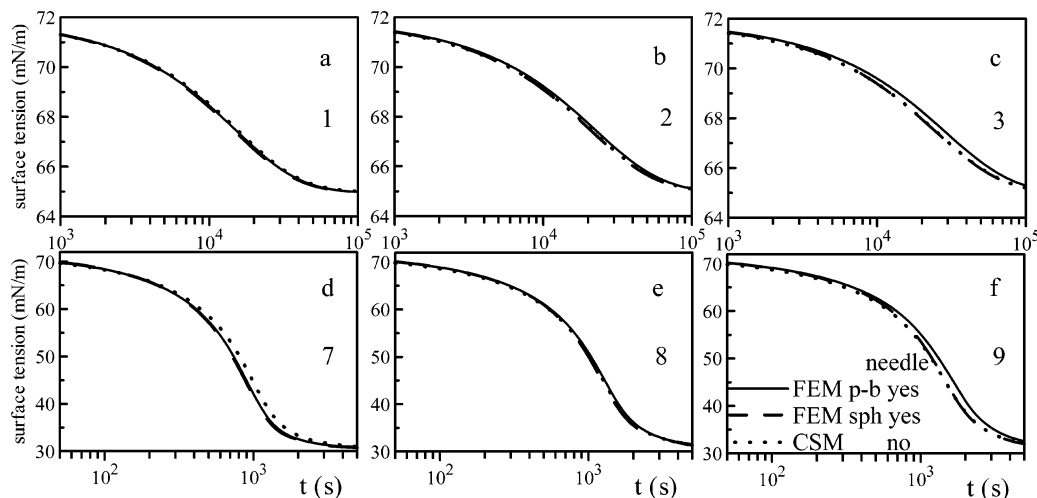


Figure 5. Comparison of DST profiles from the CSM (dotted curves) and from the FEM for spherical bubbles with the needle (dashed curves, sph) and for pendant bubbles (solid curves, p-b) for cases 1 (a), 2 (b), 3 (c), 7 (d), 8 (e), and 9 (f), detailed in Table 1.

needle) is caused by the mass flux acceleration due to the existence of a needle. Recall here that the CSM predicts the DST without a needle.

The simulation data for a large pendant bubble (with a large $-B$, solid curves) show a slower DST relaxation (Figure 5c and f) than that of the CSM (dotted curves) or a spherical bubble with a needle (dashed curve). These data show the shape effect on bulk diffusion: the rate of diffusion onto a pendant bubble is significantly different from that onto a perfectly spherical surface. Recall that the needle effect is negligible for a large bubble (with a large $-B$).

The deviations of the DST between the FEM of a pendant bubble (solid curves) and the CSM (dotted curves) for $C_0/a = 0.5$ (Figure 5c), 2.5, and 10 (Figure 5f) are nearly identical. These nearly same deviations indicate that bulk concentration plays only a minor role here.

In summary, needle size and bubble shape are the two major factors that affect the DST for surfactant bulk diffusion. The existence of a needle accelerates bulk diffusion for a small bubble (Figure 5d). However, a flatter pendant bubble profile (large $-B$) decelerates the bulk diffusion. These two factors may counterbalance each other under certain conditions. For example, Figure 5e shows a nearly same DST profile for the pendant bubble FEM as well as the CSM. Note that, in Figure 5c and f, the deceleration dominates the DST relaxation for a large pendant bubble.

The CSM has been applied to interpret the DST data measured using pendant bubble technique for several surfactants.^{6,18–20} When the mass transport is a diffusion-controlled process, diffusivity is the only unknown parameter. Diffusivity can then be evaluated from the best-fit between the experimental DST data and the theoretical DST profiles from the CSM. In the following work, a constant diffusivity, $D = 5.0 \times 10^{-6} \text{ cm}^2/\text{s}$, is utilized for theoretical simulations.

Fitting Using the CSM. We assume that the pendant bubble FEM with a needle predicts the exact DST profiles, and one applies the CSM without a needle to simulate the bulk diffusion of surfactant. Figure 6 shows that the CSM can predict the DST profiles perfectly, however, with a different diffusivity. For a small bubble (Figure 6a), a larger diffusivity ($5.3 \times 10^{-6} \text{ cm}^2/\text{s}$) results from the CSM. Note that the solid curves have a diffusivity of $5.0 \times 10^{-6} \text{ cm}^2/\text{s}$. In other words, the needle effect causes an $\sim 6\%$ deviation in the diffusivity when one applies the CSM to simulate the DST profiles.

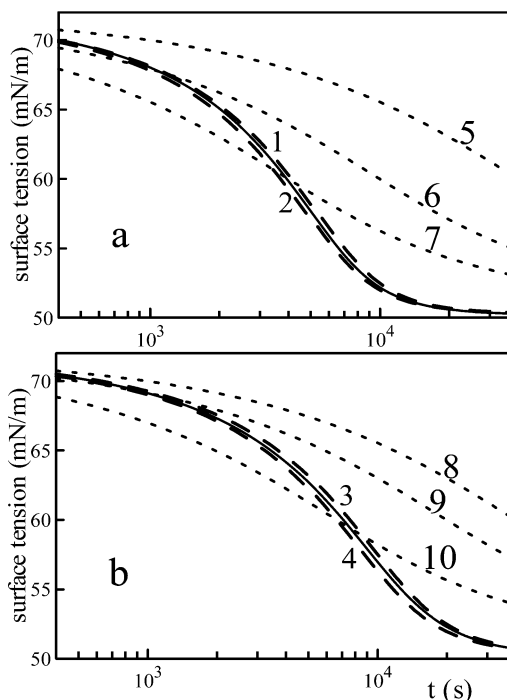


Figure 6. DST profiles from the pendant bubble FEM (solid curves; case 4 (a) and case 6 (b) in Table 1; $D = 5.0 \times 10^{-6} \text{ cm}^2/\text{s}$) and from the CSM (dashed curves 1–4). $D = 5.0$ (1), 5.6 (2), 4.2 (3), and 4.8 (4) [$10^{-6} \text{ cm}^2/\text{s}$]. Dotted curves 5–10 are the DST for a planar surface with $D = 5.0$ (5 and 8), 20 (6), 50 (7), 10 (9), and 30 (10) [$10^{-6} \text{ cm}^2/\text{s}$].

For a large pendant bubble (as illustrated in Figure 6b), the CSM results in a diffusivity of $4.5 \times 10^{-6} \text{ cm}^2/\text{s}$. A 10% error results from the shape effect of a fluid–liquid interface for the case in Figure 6b. Figure 7 gives a summary on the error of diffusivity when one applies the CSM to fit the exact DST profiles. The CSM underestimates the diffusivity by 10–12% for a large bubble and overestimates the diffusivity by 6–10% for a small bubble.

Note that if the air–water surface is assumed to be planar, the DST shows a quite different relaxation (the dotted curves in Figure 6) and a much larger diffusivity results from the best-fit with the DST data (solid curves). A DST profile from a planar surface may fit the DST data in a small time region quite well. However, a larger diffusivity may result, and the deviation is dependent upon the surfactant bulk concentration.

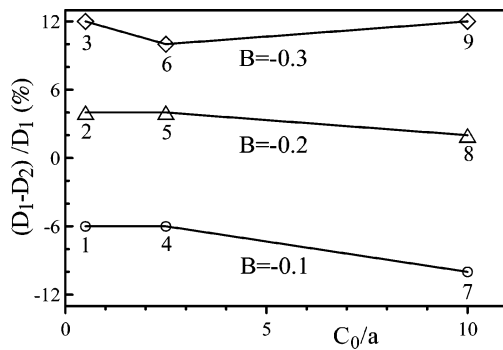


Figure 7. Relative diffusivity difference between the pendant bubble FEM (D_1 , with a needle) and the best-fit diffusivity from CSM (D_2 , without a needle) at various surfactant concentrations. The number under the symbol indicates the case number listed in Table 1 or Figure 3.

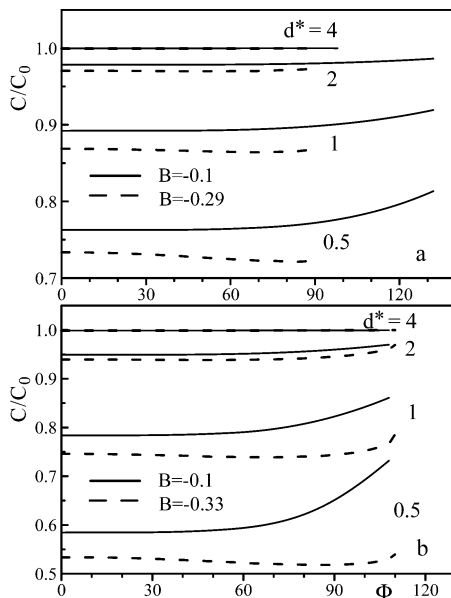


Figure 8. Bulk concentration profile along angle Φ at different solution depths d^* at $t^* = 1.0$: $-B = 0.1$ (solid curves) and $-B = \sim 0.3$ (dashed curves); $C_0 = 2.0 \times 10^{-10}$ (a) and 4.0×10^{-9} (b) mol/cm^3 .

Bulk Concentration Profile. Figure 8 illustrates an example of the bulk concentration profiles at different positions in solution space and at dimensionless time $t^* = 1$ (here, $t^* = Dt/h_p - b^2$). Since the surfactant concentration $C(x, y, z, t)$ is axis-symmetric, only two variables, $C(r, \theta, t)$, are needed to specify the concentration in the bulk phase. The dimensionless adsorption depth d^* ($= (R_0^* - R_0)/h_p - b$) and an angle Φ are utilized in this study.

The dimensionless d^* indicates the distance away from the air–water interface, as shown in Figure 1. A second spatial variable, angle Φ , in the bulk phase is defined as the direction passing the point ($x = 0, z = R_0$) and the interface with turning angle Φ . Note that the apex (at $x = 0, z = 0$) has zero ϕ and $\Phi = 0$ indicates a position right below the apex.

For the solution far away from the air–water interface (at large d^*), the surfactant concentration in the bulk phase is quite uniform in all directions of different Φ . At small d^* (bulk regions close to the bubble surface), an increase in bulk concentration is observed at large Φ . This increase becomes significant when the bulk concentration of surfactant solution is high.

A decrease in bulk concentration with Φ was also observed for large bubbles. For example, at $-B = 0.29$, the concentration

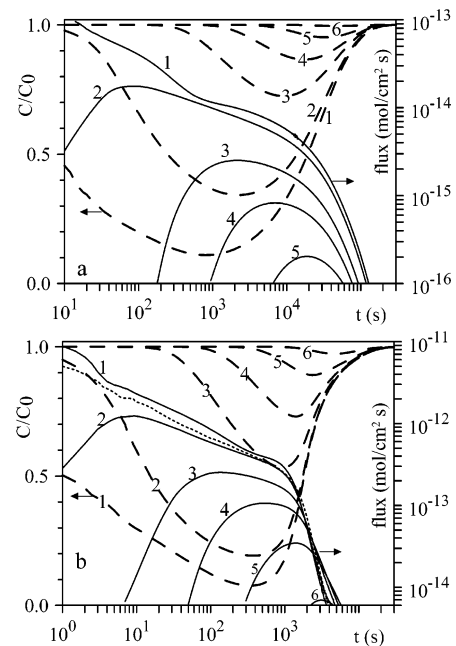


Figure 9. Dynamic bulk concentration (dashed curves) and diffusion flux (solid curves) at various solution depths at zero Φ for case 3 (a, $C_0/a = 0.5$) and case 9 (b, $C_0/a = 10$), listed in Table 1. Solution depth $d^* = 0.01$ (1), 0.1 (2), 0.5 (3), 1 (4), 2 (5), and 4 (6). The dotted curve shows the relaxation of adsorption flux at the air–water surface.

profile near the bubble surface ($d^* = 0.5$ and 1.0) shows a small decrease at the beginning and then increases with increasing Φ . This variation of the bulk concentration is probably due to the effect of the local shape of the pendant bubble on the diffusion flux.

The concentration increase in the large Φ section indicates the needle effect. Surfactants cannot diffuse and adsorb onto the needle wall (boundary conditions 4f); surfactants therefore diffuse and adsorb onto the bubble surface adjacent to the tip of the needle. Thus, a higher surfactant concentration results at the bulk region close to the needle. This has been also discussed in above section: the needle effect is more significant for a small bubble (Figure 8, bubble with $-B = 0.1$). However, for the bulk region far enough away from the bubble surface ($d^* > 1$), the needle effect becomes nearly negligible.

Figure 9 demonstrates the dynamic bulk concentration at various solution depths (d^*) at zero Φ for a diffusion-controlled adsorption process. The limited bulk diffusion causes a decrease in surfactant concentration at a short time, and then it relaxes and comes back to the initial bulk concentration C_0 as the system reaches equilibrium. The decrease of C/C_0 at a specific d^* indicates that the bulk diffusion rate ($ADVC$) of the surfactant to this position is smaller than that from this position to the subsurface at this time. C/C_0 increases with time when the bulk diffusion rate to this point is larger than that from this point to the subsurface. It takes a longer time for the C/C_0 profile to reach its minimum for a larger d^* (farther away from the bubble surface). A dilute solution also takes a longer time for the adsorption onto a freshly created bubble surface to reach its equilibrium state.

Figure 9 shows also the diffusion flux (per surface area) at various d^* at zero Φ . In general, the flux increases with time, reaches a maximum, and then decreases at the time when the surface tension relaxation is leveling off. There is a larger flux at smaller d^* , the region close to the air–water surface. Both the C/C_0 and diffusion flux curves specify the region of the mass

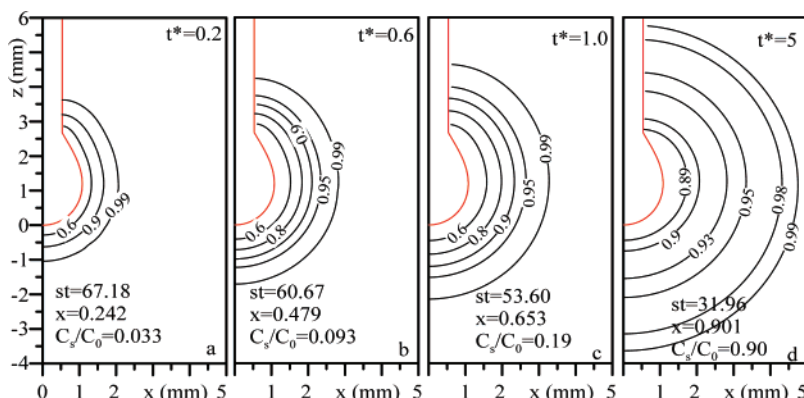


Figure 10. Dimensionless concentration contours outside the pendant bubble for case 9 at time $t^* = 0.2, 0.6, 1.0,$ and 5 , where $t/t^* = 1019$ s.

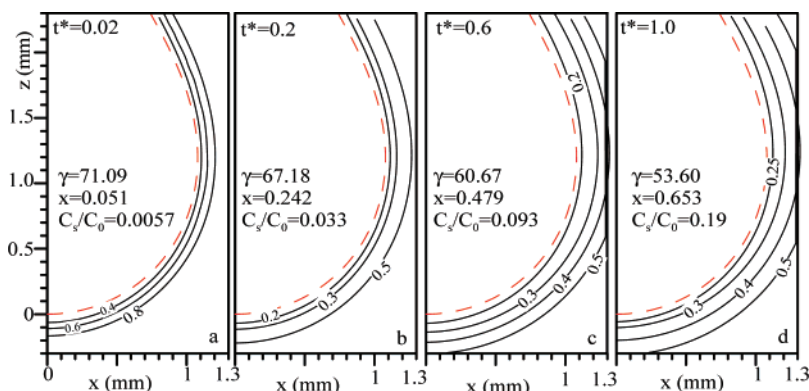


Figure 11. Dimensionless concentration contours in the neighborhood of the pendant bubble surface (dashed curves) for case 9 at time $t^* = 0.02, 0.2, 0.6,$ and 1.0 .

transport wave due to the sudden creation of a pendant bubble (i.e., a certain area of the air–water interface) inside a bulk solution.

The dotted curve in Figure 9 indicates the adsorption flux at the surface, which is the average of the adsorption flux at all different Φ . The dotted curve is very close to, but smaller than, the one at $d^* = 0.01$ and $\Phi = 0$. This implies that the diffusion flux in the direction of $\Phi = 0$ is a little larger than the average diffusion flux at $t < 1000$ s. It is noted that the diffusion flux varies slightly at various Φ .

The corresponding dimensionless concentration contours outside the pendant bubble for case 9 (listed in Table 9) are plotted in Figure 10 at dimensionless time $t^* = 0.2, 0.6, 1.0,$ and 5 . Note that $t/t^* = 1019$ s for case 9. The contours close to the bubble surface are enlarged in Figure 11 for $t^* = 0.02, 0.2, 0.6,$ and 1.0 . Figure 10 shows that the depleted surfactant region (for example, the region for $C/C_0 < 0.99$) grows with time. At $t = 200$ s, it is only about 1 mm (the size of the bubble radius), and γ reaches 67 mN/m at this time. It increases to 2.2 mm at $t = 1000$ s and even reaches to around 3.6 mm at $t = 5000$ s. Note that the depleted region becomes thinner at the end of the mass transport process.

Figure 11 shows the variation of the surfactant concentration adjacent to the bubble surface. At $t = 20$ – 200 s, the surfactant concentration adjacent to the bubble surface decreases with time (see also curve 1 in Figure 9) and the depleted surfactant region increases quickly. Note that the subsurface concentration also decreases with time during this time period.

The depletion of the surfactant concentration in the bulk phase is due to the bulk diffusion onto a freshly created bubble surface, first into the region adjacent to the bubble surface and then deeper into the bulk phase. A solution depth d^* in the bulk phase, where

the surfactant concentration is depleted by 5% ($C/C_0 = 0.95$), is defined as d_{95}^* . In other words, d_{95}^* is a simple index on how deep the bulk solution is for the surfactant adsorption process at that specific time. In a similar way, one can define d_{90}^* and d_{99}^* for a solution depth d^* in the bulk phase where the surfactant concentration is depleted by 10% and 1%, respectively.

Figure 12 demonstrates the dynamic d_{95}^* at two different angles of pendant bubbles. At dilute concentrations ($C_0/a = 0.5$ for curves a–d in Figure 12a), the maximum d_{95}^* is roughly twice the adsorption depth. At a higher concentration ($C_0/a = 10$ for curves e–h in Figure 12b), 3 times the adsorption depth is needed for the maximum d_{95}^* . Besides, a bubble with a larger $-B$ (dashed curves in Figure 12) has a larger maximum d_{95}^* .

Someone may prefer using the position with $C/C_0 = 0.90$ or 0.99 as the affected depletion depth. Figure 13 illustrates the effects of the capillary constant and bulk concentration on the maximum d_{90}^* , d_{95}^* , and d_{99}^* . The maximum d_{90}^* , d_{95}^* , and d_{99}^* values go up to around 2, 3, and 4.8, respectively.

The dynamic d_{95}^* increases with time, reaches a maximum, and then relaxes and comes back to zero. The relaxation of d_{95}^* indicates the depth of the mass transport wave, that is, the region with significant surfactant concentration depletion in the bulk phase. The maximum value of the dynamic d_{95}^* or d_{99}^* curve is therefore the minimum solution depth required for a surfactant solution being designed for this solution system to be claimed as “a pendant bubble in an infinite solution system”.

8. Illustration Example of $C_{12}E_4$

DST profiles of nonionic surfactant $C_{12}E_4$ solutions are utilized to examine the present FEM model since the Langmuir isotherm

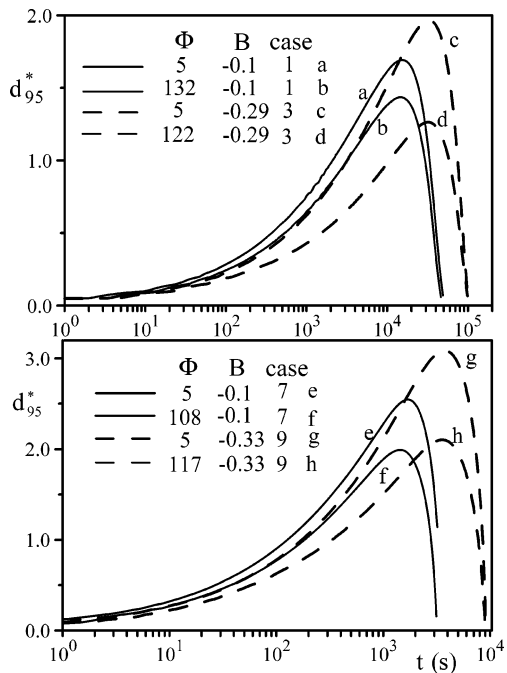


Figure 12. Dynamic 95% depletion depth of pendant bubbles at a small and a large Φ for runs 1, 3, 7, and 9, listed in Table 1.

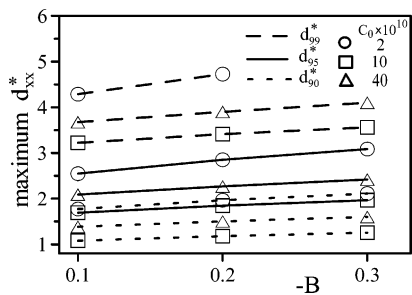


Figure 13. Maximum d_{90}^* , d_{95}^* , and d_{99}^* as a function of capillary constant B and bulk concentration C_0 for the cases listed in Table 1.

fits the DST data of $C_{12}E_4$ reasonably well.^{34,35} The model constants for $C_{12}E_4$ at 25 °C are $\Gamma_\infty = 3.90 \times 10^{-10}$ mol/cm² and $a = 4.66 \times 10^{-10}$ mol/cm³, which were obtained by minimizing the deviation between the experimental equilibrium data and theoretical curves.

The shape of a pendant bubble relaxes with time during the surfactant adsorption process, and even the bubble volume keeps nearly constant. Illustrated in Figure 14 is a representative example for the relaxation of capillary constant during the surfactant adsorption process. In this run of 6.0×10^{-9} mol/cm³, the capillary constant B varies from -0.23 to -0.31 . This indicates a bubble elongation and a decrease of surface tension during this process. A capillary constant of -0.31 was used for the FEM numerical simulation in this case.

The diffusivity of $C_{12}E_4$ can be obtained from the DST data in Figure 15. Theoretical DST profiles from the FEM (solid curves) and CSM (dashed curves) were computed by adjusting the diffusivity to achieve the best-fit with the experimental DST data. DST at two bulk concentrations, 6×10^{-9} and 10×10^{-9} mol/cm³, were used, and the diffusivities that resulted from the FEM are roughly 10% higher than those from the CSM. The fitting between the other DST data of different surfactant concentrations and the corresponding theoretical curves has a

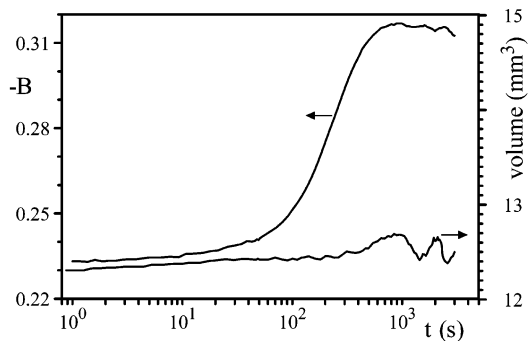


Figure 14. Relaxation of the capillary constant and bubble volume for a pendant bubble of $C_{12}E_4$ during surfactant adsorption for $C_0 = 6 \times 10^{-9}$ mol/cm³.

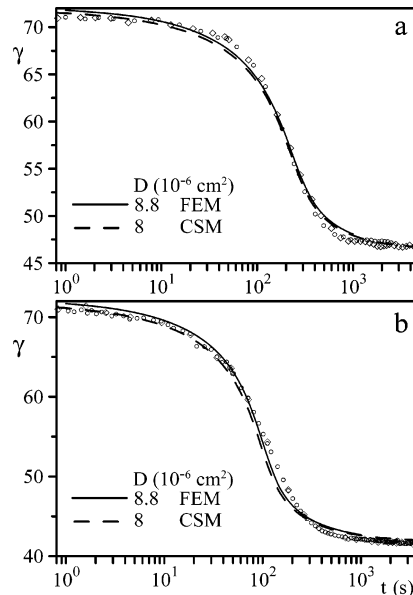


Figure 15. DST data for $C_{12}E_4$ adsorption onto a freshly created air–water interface and the best-fit theoretical curves from FEM (solid curves) and CSM (dashed curves) for $C_0 = 6$ (a) and 10 (b) [10^{-9} mol/cm³].

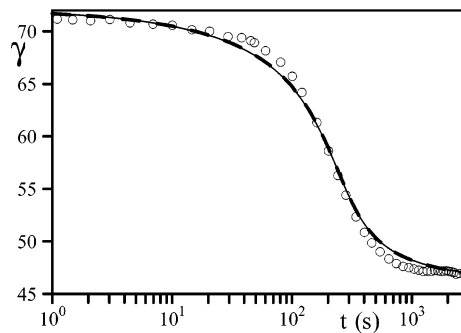


Figure 16. Comparison between the DST profiles predicted using R_0 and B at $t = 100$ s ($R_0 = 1.30$ mm, $B = -0.235$; dashed curve) and $t = 3000$ s ($R_0 = 1.22$ mm, $B = -0.310$; solid curve) for $C_0 = 6 \times 10^{-9}$ mol/cm³. Circles represent the measured DST data.

nearly same result. This 10% increase is similar to the results shown in Figure 7 (cases 3, 6, and 9) for bubbles with large $-B$.

In practice, pendant bubbles deform under gravity during dynamic surface tension measurements. In Figure 14, the capillary constant ($-B$) remains nearly constant for $t < 50$ s at this concentration, where γ goes down slowly also. R_0 , $-B$, and γ all level off at large times, where the mass transport process approaches nearly the equilibrium state. A dramatic increase of

(34) Hsu, C. T.; Shao, M. J.; Lin, S. Y. *Langmuir* **2000**, *16*, 3187.
 (35) Hsu, C. T.; Shao, M. J.; Lee, Y. C.; Lin, S. Y. *Langmuir* **2000**, *16*, 4846.

$-B$ takes place at a short time (100–400 s) region, where γ decreases dramatically.

To evaluate the effect of bubble deformation on DST, two sets of R_0 and $-B$ were chosen for the FEM simulation. One set is the values at equilibrium, and the other is those at $t = 100$ s, where R_0 , $-B$, and γ start to change abruptly. Figure 16 shows the DST profiles for these two sets of parameters for $C_{12}E_4$. These two DST profiles are nearly identical. Similar results are also observed for the other three $C_{12}E_4$ concentrations. Therefore, bubble deformation (shown by the change of $-B$ and R_0) during the surfactant adsorption process has a negligible contribution to DST.

9. Conclusion and Discussions

A finite element method (FEM) for simulating surfactant adsorption onto a freshly created pendant bubble was successfully applied to analyze the adsorption kinetics of a diffusion-controlled process. The FEM applied to the surfactant adsorption process in this study was based on the pendant bubble shape and needle used in the experimental measurements.

The simulation results indicate that the needle size and bubble shape are the two major factors affecting the DST of the surfactant bulk diffusion process. The existence of a needle, where a pendant bubble is hanging on the tip, accelerates the bulk diffusion for a small bubble. However, the shape of a large pendant bubble decelerates the bulk diffusion.

Furthermore, the FEM is capable to study the relaxation of the surfactant concentration in the bulk phase. One is therefore able

to monitor the flux and direction of the surfactant diffusion process by using the FEM.

When one uses the classical spherical model (CSM) to simulate the DST data, the CSM may underestimate the diffusivity by 10–12% for a large pendant bubble and overestimate the diffusivity by 6–10% for a small bubble. The DST data of $C_{12}E_4$ was also used to verify this phenomenon at the end of the above section.

In this work, the Langmuir adsorption isotherm was applied for modeling the adsorption/desorption behavior. Since the molecular interaction between the adsorbed surfactants has been verified to be important for many surfactants, the use of an isotherm including the intermolecular interaction forces should be considered. The study using the Frumkin adsorption isotherm is now in process in our lab.

It is noted that the simulation in this study will work only for the diffusion-controlled mass transport of nonionic surfactants with $C < \text{cmc}$. For ionic surfactants with significant ionic forces between surfactant molecules,^{36,37} the assumptions of diffusion control and the Langmuir adsorption isotherm used in this work may fail.

Acknowledgment. This work was supported by the National Science Council of Taiwan under Grant NSC 89-2214-E-011-021.

LA701978W

(36) Diamant, H.; Andelman, D. *J. Phys. Chem.* **1996**, *100*, 13732.

(37) Mohrbach, H. *J. Chem. Phys.* **2005**, *123*, 126101.